



Article

Hydrogen Embrittlement Behavior of Plastically Pre-Strained and Cathodically Hydrogen-Charged 316H Grade Austenitic Stainless Steel

Ladislav Falat ^{*}, Lucia Čiripová , Ivan Petryshynets, Ondrej Milkovič, Miroslav Džupon and Karol Kovaľ

Institute of Materials Research, Slovak Academy of Sciences, Watsonova 47, 04001 Košice, Slovakia

^{*} Correspondence: lfalat@saske.sk; Tel.: +421-55-792-2447

Abstract: In this work, the effects of electrochemical hydrogen charging of 316H grade austenitic stainless steel were investigated in order to characterize its hydrogen embrittlement (HE) resistance. The as-received 316H material was in a fully recrystallized (solution-annealed) material condition. The susceptibility to HE of the studied material was evaluated by determination of the embrittlement index from the results of conventional uniaxial tensile tests of nonhydrogenated and hydrogen-charged test specimens. The study was focused on the effects of two selected plastic pre-strain levels of tensile specimens on their resulting HE resistance. The selected pre-strains corresponded to the tensile stress conditions within the “yield stress–ultimate tensile strength” (YS–UTS) range and directly at the UTS point. The obtained embrittlement indices for the presently used pre-straining and hydrogen charging conditions indicated that the HE of the studied material states was small. However, it was revealed that the observed degradation of deformation properties of plastically pre-strained and hydrogen-charged materials was mainly caused by gradual plasticity exhaustion due to tensile straining, which well correlated with the observed effects indicated by electron backscatter diffraction analyses and indentation hardness measurements.

Keywords: austenitic steel; hydrogen embrittlement; microstructure; tensile test; fractography



Citation: Falat, L.; Čiripová, L.; Petryshynets, I.; Milkovič, O.; Džupon, M.; Kovaľ, K. Hydrogen Embrittlement Behavior of Plastically Pre-Strained and Cathodically Hydrogen-Charged 316H Grade Austenitic Stainless Steel. *Crystals* **2022**, *12*, 1419. <https://doi.org/10.3390/cryst12101419>

Academic Editors: Yang Liu, Vasilis Karamitros and Mingyi Zheng

Received: 27 September 2022

Accepted: 6 October 2022

Published: 8 October 2022

Publisher's Note: MDPI stays neutral with regard to jurisdictional claims in published maps and institutional affiliations.



Copyright: © 2022 by the authors. Licensee MDPI, Basel, Switzerland. This article is an open access article distributed under the terms and conditions of the Creative Commons Attribution (CC BY) license (<https://creativecommons.org/licenses/by/4.0/>).

1. Introduction

The group of “300 series stainless steels” involves a wide range of austenitic stainless steels with the matrix phase possessing a face-centered cubic (FCC) crystal structure thanks to their specific chemical composition involving high alloying with austenite-stabilizing nickel. These high-alloyed chromium-nickel steels, originally derived from traditional 18Cr/8Ni stainless steel, are frequently used in a wide range of structural applications covering various industrial and civil branches [1–7]. The 316H grade (18Cr-12Ni-2Mo, high C) represents one of the most common austenitic stainless steels with additional alloying by molybdenum to assure its higher corrosion resistance [8]. Compared to other grades of “300 series stainless steels”, the increased carbon content in 316H grade (up to 0.08 wt.% C) makes this material more resistant to creep loading and, thus, suitable for structural applications in high-temperature service environments [9–13]. A typical application of 316H steel grade involves high-temperature steam tubing within superheater and reheater portions of so-called “ultra-supercritical” boilers in modern highly efficient and ecologically friendly thermal power plants [14–16]. The use of 316H steel also includes structural parts in nuclear power generation equipment [17–19]. In specific constructional places, dissimilar welded joints, i.e., the welded joints between various steel grades, are frequently used to create functional inter-connections of consecutive circuits.

Our previous works [20–27] dealt with dissimilar weldments between the austenitic TP316H steel and various grades of high-chromium tempered martensitic steels. Apart from our studies that focused on the creep behavior and mechanical properties of such weldments [21,22,24–26], separate investigations about the susceptibility of these weldments to

hydrogen embrittlement (HE) were also performed [20,23,27]. The issue of HE can be considered relevant in operational conditions involving the regular or accidental shut-down of power generation plants and cooling down of the boiler equipment below 150 °C [28]. The dissolved atomic hydrogen that possibly entered the steel microstructure from supercritically heated and pressurized steam may further lead to hydrogen-induced cracking (HIC) in the presence of tensile stresses. Generally, a small quantity of hydrogen is sufficient to cause failures because it can magnify its effect by migrating to high-triaxial-stress regions [29]. The results obtained from our previous investigations [23,27] on dissimilar T91/TP316H and T92/TP316H weldments indicated that the applied electrochemical hydrogenation did not strongly affect their strength properties but resulted in a clear reduction in their deformation properties. The combined effects of thermal exposure and subsequent hydrogen charging on the mechanical properties of the studied weldments were more complex. With increasing time of thermal exposure, the HE manifestations were partly suppressed thanks to additional thermally induced precipitation of fine secondary phases that acted as irreversible hydrogen traps. On the other hand, with increasing ageing time, the dominance of thermal embrittlement was clearly indicated in weldments without application of hydrogen charging [23,27]. Regarding the failure locations of dissimilar T92/TP316H weldments after the combined effects of thermal exposure, hydrogen charging, and tensile straining, it has been concluded that the most critical regions of the weldments represent weld metal interfaces directly at or in close vicinity of the weld metal/base metal fusion boundary [27].

Concerning the investigations on HE of 316 type steel base material, it should be noticed that there are a significant amount of data available in the literature, e.g., [30–43], mostly focused on 316L grade, i.e., the 316 steel low-carbon version (up to 0.03 wt.% C). Apart from that, it has been often shown that observable variations in the phase composition and properties of materials and structures based on 316 type steel may strongly depend even on slight compositional variations of individual melts, their purity, processing, and final quality treatment conditions, playing a key role affecting the resulting material characteristics. Thus, it is always worth studying specific material states of 316 type steels individually.

In the present work, the effects of cathodic hydrogen charging of 316H grade austenitic stainless steel were investigated in order to characterize its hydrogen embrittlement (HE) resistance. The determination of HE index from room-temperature tensile tests of non-hydrogenated and hydrogen-charged test specimens involved the effects of two applied plastic pre-strain levels. The observed effects of tensile pre-strain and hydrogen charging on the mechanical properties and fracture behavior of the studied material states were characterized and discussed.

2. Materials and Methods

Commercial 316H austenitic stainless steel in the form of a seamless tube with a 38 mm outside diameter and 6 mm wall thickness was used as experimental material. Its chemical composition is shown in Table 1.

Table 1. Chemical composition in wt.% of the investigated 316H steel.

Material	C	Si	Mn	Cr	Mo	Ni	Fe
316H	0.05	0.51	1.77	16.76	2.05	11.13	Rest

The susceptibility of the studied material to HE was determined from the results of conventional uniaxial tensile tests of nonhydrogenated and electrochemically hydrogen-charged tensile test specimens. Cathodic hydrogen charging was carried out at ambient temperature for 24 h in electrolytic solution of 1 M HCl with 0.1 N N₂H₆SO₄ at a current density of 200 A/m². These electrochemical hydrogenation conditions have been optimized with respect to hydrogen charging time in our former study [20] that indirectly indicated

hydrogen saturation of tensile test specimens via the unchanging course of the measured deformation properties of tensile test specimens of alloy steels' welded joints hydrogenated beyond 24 h of hydrogen charging time. Moreover, according to other published studies, e.g., [44–46], full hydrogen saturation of tensile test specimens after 24 h of hydrogen charging was directly determined by hydrogen concentration measurements. While Yin et al. [47] indicated that the diffusible hydrogen concentration tends to reach the saturation state when the hydrogen charging time reaches 48 h, the study showed the difference in diffusible hydrogen contents for 24 h and 48 h hydrogen charging to be negligible. After the hydrogen charging, the tensile test specimens were stored in a thermal insulating flask filled with liquid nitrogen and consecutively subjected to room-temperature tensile testing. The overall procedure for HE resistance determination was the following: Three tensile test specimens for each material condition (i.e., nonhydrogenated and hydrogen-charged) were subjected to room-temperature uniaxial tensile testing employing a universal testing machine TIRATEST 2300 (TIRA GmbH, Schalkau, Germany) at a cross-head speed of 0.2 mm/min. After performing the tensile tests, average values of mechanical properties, i.e., yield stress (YS), ultimate tensile strength (UTS), total elongation (EL), and reduction in area (RA), were determined for nonhydrogenated and hydrogen-charged conditions. The YS was estimated as 0.2% proof stress. The HE index was calculated as a relative change in average values of area reduction between nonhydrogenated and hydrogen-charged tensile test specimens. Cylindrical tensile test specimens with M6 threaded head portions were used in the present investigation (see Figure 1).

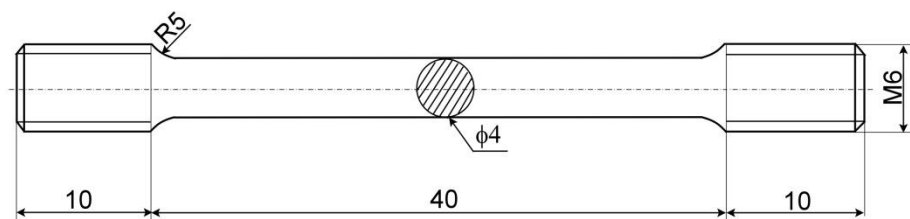


Figure 1. Cylindrical tensile test specimens (all dimensions are in mm).

In order to determine the effect of plastic pre-strain on the HE of the studied material, two different plastic pre-strain levels were applied to further sets of tensile test specimens. Figure 2 schematically shows the experimental design philosophy for the selection of plastic pre-strain levels in the context of engineering a stress–strain diagram. The pre-strain levels were individually selected to correspond with tensile stress conditions either within the YS–UTS range or directly at the UTS point.

Microstructural and fractographic analyses of the studied test specimens were performed using a scanning electron microscope (SEM) JEOL JSM-7000F (Jeol Ltd., Tokyo, Japan) equipped with an electron backscatter diffraction (EBSD) detector Nordlys-I (HKL technology A/S, Hobro, Denmark). The EBSD analyses were performed on a drawing direction plane (540 μm by 420 μm in size) of prepared metallographic specimens in various material conditions (i.e., as-received, pre-strained, and hydrogen-charged) and the obtained EBSD data were processed by the CHANNEL-5, HKL software package (Service pack 7). Fractographic observations of broken tensile test specimens were carried out using secondary electrons imaging (SEI) mode in the SEM.

The X-ray diffraction (XRD) phase analysis of the studied material under the selected material conditions was carried out by a Philips X'Pert Pro diffractometer (Panalytical B.V., Almelo, The Netherlands) in Bragg–Brentano geometry, using Cu–K α radiation and an ultra-high-speed detector X'Celerator (type number: 9430 030 15201, Malvern Panalytical Ltd., Malvern, UK).

The as-received and pre-strained material states in both their nonhydrogenated and hydrogen-charged conditions were complementarily subjected to microhardness tests and nanoindentation measurements using the microhardness tester WILSON-WOLPERT Tukon 1102 (Buehler ITW Co, Lake Bluff, IL, USA) and the nanoindenter Agilent G200 (Agilent

Technologies, Inc., Chandler, AZ, USA), respectively. Microhardness measurements were performed according to the ISO 6507–1:2018 standard [48] using a diamond Vickers indenter under the load of 50 gf (cca. 0.49 N) for a loading time of 15 s per measurement point. Nanohardness measurements were performed according to the ISO 14577–1:2015 standard [49] using a diamond Berkovich tip. A load-controlled indentation method was used with a maximum load of 50 μ gf (cca. 4.9×10^{-7} N). The loading time to reach the maximal load and the dwell time at the maximal load were 15 s and 10 s, respectively. Altogether, the matrix of 5×6 measurement points with 100 μ m spacing was analyzed.

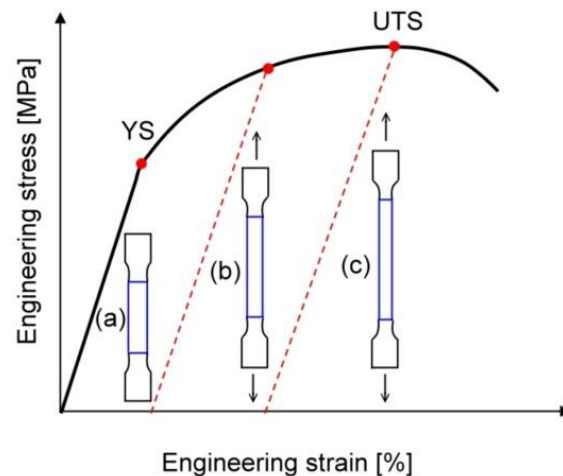


Figure 2. Experimental design philosophy for selection of plastic pre-strain levels applied to tensile test specimens in context of schematic engineering stress–strain diagram: (a) initial (unstrained) specimen, (b) plastically pre-strained specimen in tensile stress region between YS and UTS, and (c) plastically pre-strained specimen just at UTS.

3. Results and Discussion

3.1. Microstructure and Phase Analysis of As-Received Material

Figure 3 depicts the EBSD microstructure visualization by the inverse pole figure (IPF) of the as-received 316H material. It shows a polygonal grain structure with a nearly equiaxed grain morphology and randomly distributed crystallographic planes. The observed microstructure also shows that annealing twins of those occurrences in the microstructure are typically indicated by pairs of parallel lines representing twin boundaries.

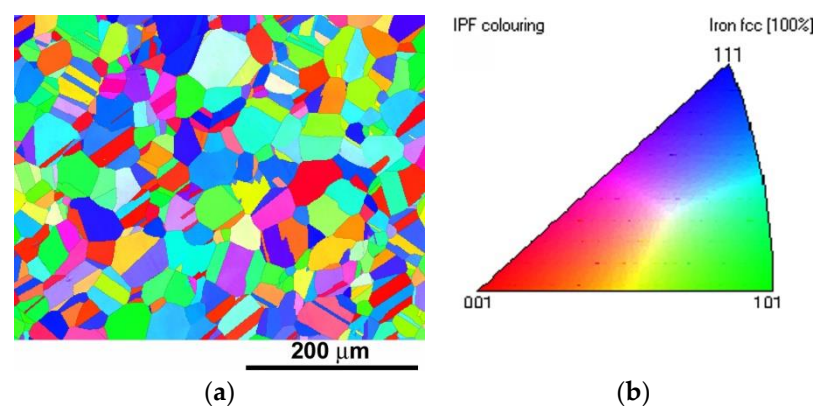


Figure 3. EBSD microstructural analysis of as-received 316H material showing: (a) Z-direction inverse pole figure and (b) corresponding IPF color key.

The XRD phase analysis of the studied 316H material in its as-received solution-annealed material condition is shown in Figure 4. The obtained XRD pattern indicates that

the studied 316H material consists of single-phase austenite, i.e., it is exclusively formed of Fe-based austenitic solid solution with an FCC crystal structure.

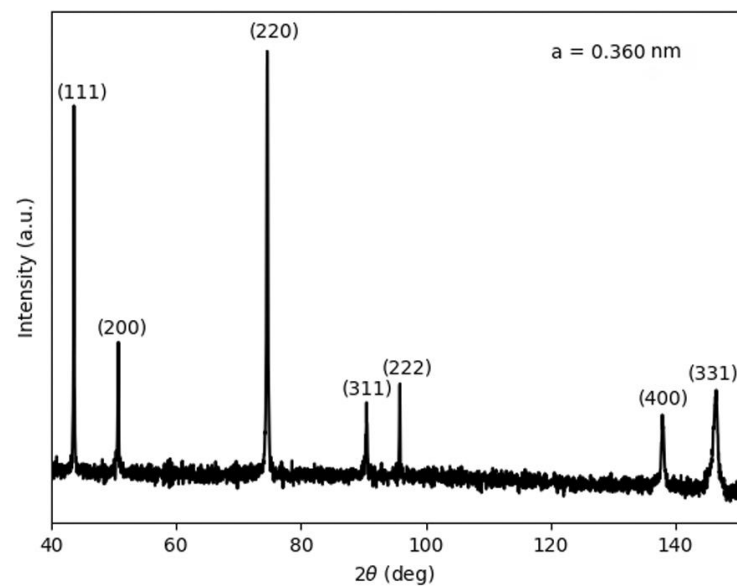


Figure 4. XRD pattern of as-received 316H material indicating its fully austenitic crystal structure, i.e., exclusively consisting of a single FCC phase solid solution with a lattice diameter of 0.360 nm.

Complementary EBSD analyses depicting the phase map (PM) and local misorientation map (LMM) are visualized in Figure 5. In accordance with the performed XRD phase analysis (Figure 4), the EBSD phase map (Figure 5a) indicates the pure FCC austenitic phase composition of the studied 316H material in its as-received solution-annealed material state. The local misorientation map in Figure 5b indicates that the as-received solution-annealed 316H material does not exhibit a considerable fraction of the areas with increased local misorientations.

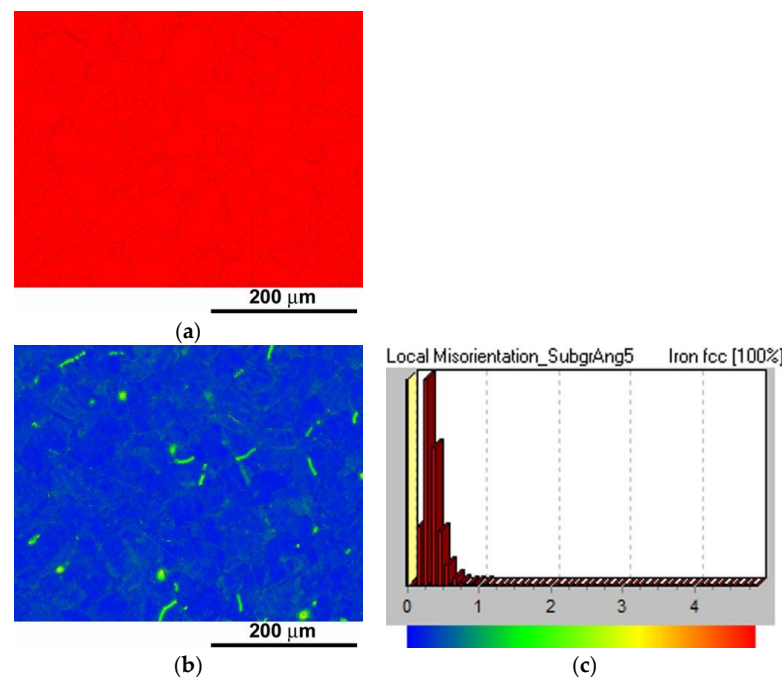


Figure 5. Complementary EBSD analyses of as-received 316H material: (a) phase map, (b) local misorientation map, and (c) corresponding LMM legend.

3.2. Effect of Hydrogen Charging on Mechanical Properties

Figure 6 shows the mechanical properties of the as-received 316H material evaluated from room-temperature tensile tests of nonhydrogenated and hydrogen-charged tensile test specimens.

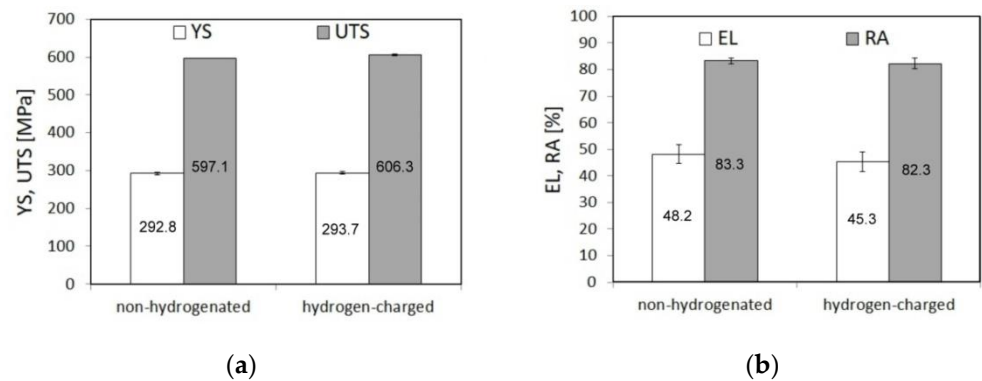


Figure 6. Room-temperature tensile properties of as-received 316H material in nonhydrogenated and hydrogen-charged material conditions: (a) strength properties: yield stress (YS), ultimate tensile strength (UTS); (b) deformation properties: total elongation (EL), reduction in area (RA).

The results in Figure 6 indicate that the performed hydrogen charging of the tensile test specimens had negligible effects on the resulting room-temperature tensile properties, compared with those of the nonhydrogenated tensile test specimens. Although a slight increase in strength properties and a certain observable decrease in deformation properties were detected for the hydrogen-charged specimens, the variation in average tensile properties was, in general, very small, i.e., within the values' scatter bands, irrespective of hydrogen charging application. Apart from the reference (initially unstrained) tensile test specimens (Figure 2a), additional plastically pre-strained test specimens (Figure 2b,c) were also examined in terms of the effect of hydrogen charging on their resulting tensile properties.

Figure 7 shows the representative engineering stress–strain diagram, obtained by the tensile test of as-received (unstrained and nonhydrogenated) 316H steel, which was used for quantitative selection of plastic pre-strain levels according to the experimental design philosophy shown in Figure 2.

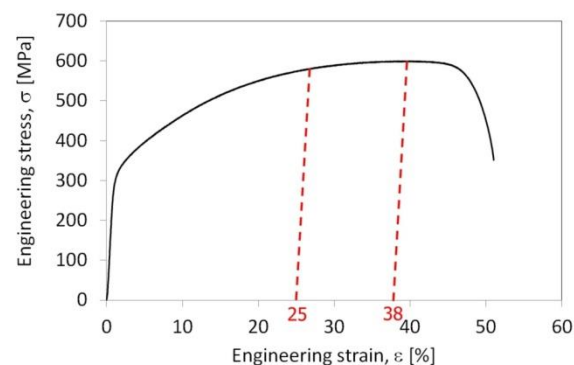


Figure 7. Representative engineering stress–strain diagram of as-received 316H steel indicating the selection of plastic pre-strain levels to be 25% and 38% in conformity with experimental design philosophy introduced in Figure 2.

According to the experimental design philosophy (Figure 2), two plastic pre-strain levels, specifically 25% and 38%, were selected on the representative engineering stress–strain curve (Figure 7) as defining pre-strain conditions for further experimental investigation. Figures 8 and 9 show the effects of the pre-straining and hydrogen charging of the studied

material on its strength and deformation properties, respectively. It can be seen that both the plastic pre-strain and hydrogen charging lead to a considerable increase in strength properties (Figure 8); however, the effect of plastic pre-strain is much more significant than the superimposing effect of hydrogen charging.

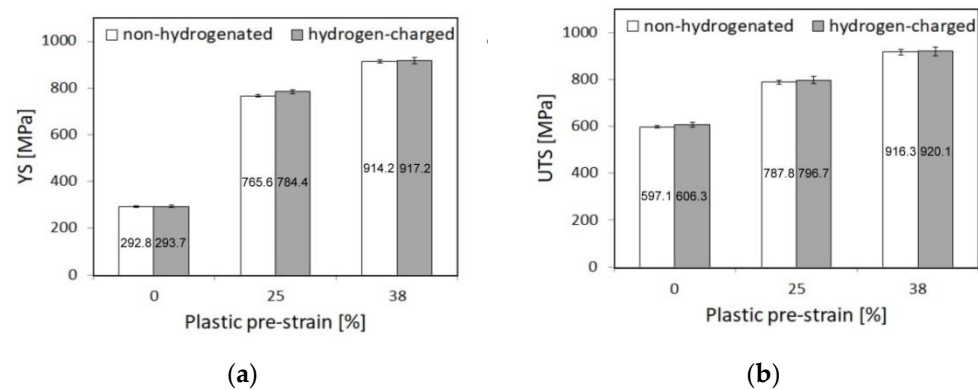


Figure 8. The effects of plastic pre-straining and subsequent electrochemical hydrogen charging of 316H steel on its strength properties: (a) yield stress; (b) ultimate tensile strength.

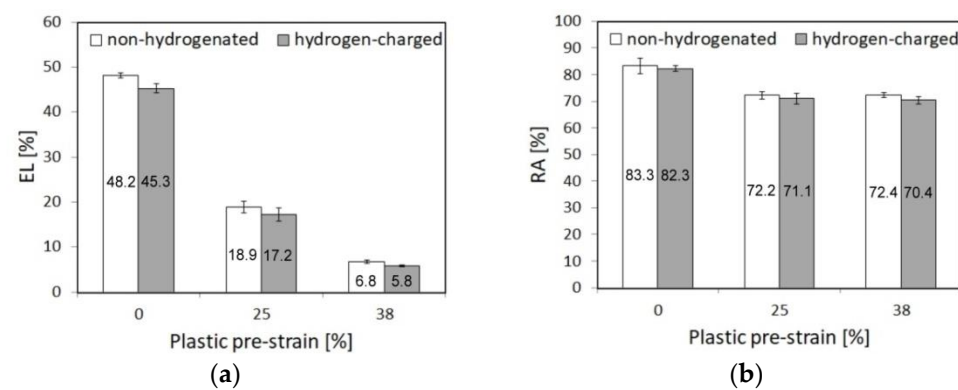


Figure 9. The effects of plastic pre-straining and subsequent electrochemical hydrogen charging of 316H steel on its deformation properties: (a) total elongation; (b) reduction of area.

On the other hand, both the plastic pre-strain and hydrogen charging lead to a considerable decrease in deformation properties (Figure 9). In this case, the effect of plastic pre-strain is also much more pronounced compared to the effect of hydrogen charging.

The obtained results clearly indicate good HE resistance of the studied material in conditions of the present investigation. Nevertheless, it holds that with the increasing level of plastic pre-strain up to 38% (corresponding to the tensile stress related to the UTS point), a clear decrease in average values of deformation properties (Figure 9) of hydrogen-charged materials is observed. It is assumed that this behavior might be attributed to the plastic pre-strain-induced microstructural changes associated with the newly formed hydrogen diffusion paths, such as strain-induced dislocations acting as reversible hydrogen trapping sites [50]. Further analyses and discussions regarding the considered microstructural effects affecting the HE resistance of the studied material are provided in the subsequent section depicting EBSD analyses of 38% plastically pre-strained material and micro/nano-indentation measurements of the unstrained and 38% plastically pre-strained materials in both the nonhydrogenated and hydrogen-charged conditions.

Fractographic characterization of broken tensile specimens did not reveal any crucial differences in fracture micro-mechanisms of individual material states (see Figure 10). All the observed fracture surfaces were characterized by the ductile dimple tearing fracture micro-mechanism. Slight differences were observed only regarding the dimple size and dimple morphology.

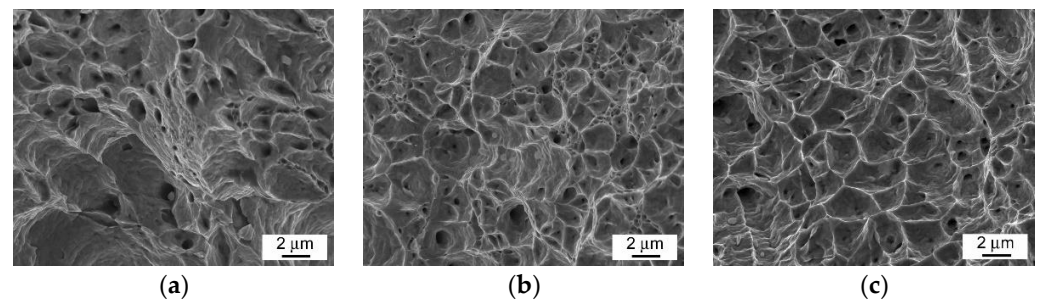


Figure 10. SEM-fractographs of fracture surfaces of broken tensile test specimens of studied 316H material in various material conditions: (a) as-received, non-hydrogenated; (b) as-received, hydrogen-charged; (c) 38% plastically pre-strained, hydrogen-charged.

By rule, the fracture surfaces of nonhydrogenated tensile test specimens exhibited somewhat larger pulled-out dimples, whereas the hydrogenated ones were characterized by smaller shallow dimples (Figure 10). The effect of pre-straining on the fracture surfaces of hydrogenated specimens was also negligible.

3.3. Hydrogen Embrittlement Evaluation

Quantitative estimation of the HE susceptibility of the studied material with different pre-strain levels was performed by calculation of the embrittlement index (EI) from average values of deformation properties (i.e., either RA or EL), according to the following equations:

$$EI_{RA} = \frac{RA_0 - RA_X}{RA_0} \times 100\% \quad (1)$$

$$EI_{EL} = \frac{EL_0 - EL_X}{EL_0} \times 100\% \quad (2)$$

The subscripts “0” and “X” refer to the initial (nonhydrogenated) and final (hydrogen-charged) material states, respectively. In order to characterize the pure effect of hydrogen charging, both the initial and final material states are considered with the same level of the plastic pre-strain. Table 2 shows the individual EI values calculated according to Equations (1) and (2).

Table 2. Hydrogen embrittlement indices of variously pre-strained 316H steel materials.

Row	0	X	EI _{RA} (0, X) [%]	EI _{EL} (0, X) [%]
1	0% pre-strain, nonhydrogenated	0% pre-strain, hydrogen charged	1.2	6.0
2	25% pre-strain, nonhydrogenated	25% pre-strain, hydrogen charged	1.5	9.0
3	38% pre-strain, nonhydrogenated	38% pre-strain, hydrogen charged	2.8	14.7

Row 1—hydrogen embrittlement of as-received (unstrained) material; row 2—hydrogen embrittlement of 25% plastically pre-strained material; row 3—hydrogen embrittlement of 38% plastically pre-strained material.

On the base of EI values in Table 2, it can be concluded that the resulting HE of the studied pre-strained 316H materials is small, although it slightly increases with the plastic pre-strain. These results indicate good hydrogen embrittlement resistance of the studied 316H material in conditions of the present investigation. It can be likely related to the high storage of plasticity in the studied material thanks to its FCC crystal structure [51,52] and also its beneficial diffusional characteristics (i.e., considerably lower hydrogen diffusivity in the FCC alloys than that in the base-centered cubic (BCC) alloys [53,54]), further enhanced by the effect of mixing entropy of the FCC solid solution as the presently investigated 316H type steel containing high concentrations of alloying elements can be regarded as a nonequiatomic medium-entropy alloy [55]. The XRD phase analyses depicting the FCC single-phase crystal structure for both the as-received (unstrained, nonhydrogenated) and 38% plastically pre-strained and hydrogen charged 316H material are shown in Figure 11.

The obtained results of the present investigation (Table 2) hold for the solution-annealed, i.e., precipitation-free, material state of the studied 316H material. It has been shown in our former studies [23,27] that grain-boundary precipitation of Cr_{23}C_6 -based carbides during high-temperature exposure of 316H material may vastly modify its hydrogen embrittlement resistance. Thus, it is emphasized that not only the chemical composition of the material but especially its specific material condition (i.e., microstructural state) is a decisive factor influencing its susceptibility to HE. Regarding the gradual increase in EI values with the increase in plastic pre-strain (Table 2), it can be assumed that this behavior is likely attributed to the plastic pre-strain-induced microstructural changes associated with the newly formed hydrogen diffusion paths, i.e., reversible hydrogen trapping sites, mainly the slip dislocations and deformation twins, possibly enhancing the HE phenomenon. In order to indicate such strain-induced microstructural changes, the EBSD microstructural analyses and micro/nano-hardness measurements were carried out.

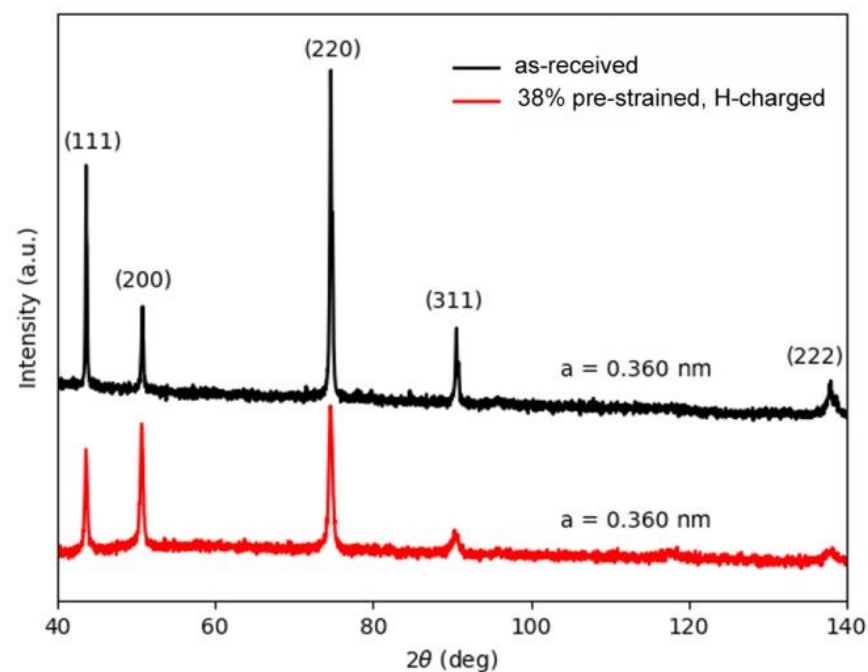


Figure 11. XRD phase analyses of as-received and 38% plastically pre-strained, hydrogen charged 316H material indicating its fully austenitic crystal structure, i.e., exclusively consisting of single FCC phase solid solution with a lattice diameter of 0.360 nm.

Figure 12 depicts EBSD microstructure visualizations by an inverse pole figure (Figure 12a) and local misorientation map (Figure 12c) of 38% plastically pre-strained 316H material corresponding to the stress–strain condition of the UTS point. Figure 12a,b indicate a longitudinally deformed grain structure with a major occurrence of $\{101\}$ crystallographic planes and distinct locations showing deformation twins that can be counted to the newly formed hydrogen diffusion paths and the places of local hydrogen accumulation [56]. Figure 12c,d highlight the areas with increased local misorientations (yellow and red areas) that indicate locally increased mechanical strains related to plastic deformation associated with an increased density of dislocations that are well-known reversible hydrogen trapping sites enhancing the measure of HE.

Moreover, by comparison of individual hydrogen embrittlement indices of variously pre-strained 316H steel materials in Table 2, it is interesting to note that the EI_{EL} indices possess clearly higher values than the EI_{RA} indices. This observation may be related to the surface degradation of tensile test specimens during the performed electrochemical hydrogenation, which affects the resulting EL values more significantly than the resulting RA values as it is well-known that surface degradation vastly deteriorates the ductility of

structural steels thanks to the earlier onset of necking on superficially degraded tensile test specimens [57]. A typical surface morphology of the hydrogenated tensile test specimen was additionally documented by SEM visualization showing some banding and pitting-like surface degradation (see Figure 13).

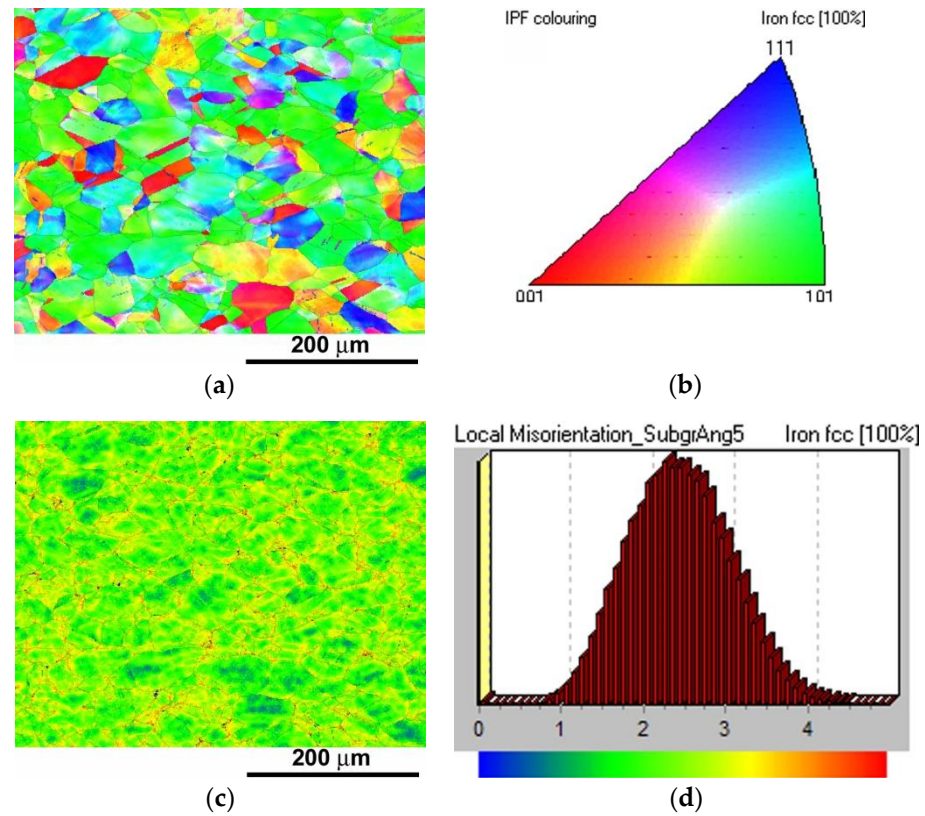


Figure 12. EBSD microstructure visualization of 38% plastically pre-strained 316H material: (a) inverse pole figure, (b) IPF color key, (c) local misorientation map, and (d) LMM legend.

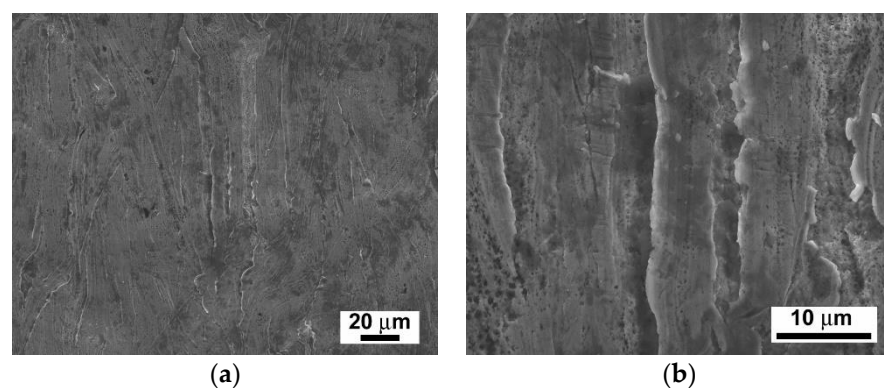


Figure 13. Typical surface degradation of hydrogenated tensile test specimen after cathodic hydrogen charging of studied 316H material visualized by SEM at: (a) lower magnification and (b) higher magnification.

Figure 14 demonstrates the effects of 38% plastic pre-strain and hydrogen charging on the results of micro-hardness and nano-hardness measurements. From Figure 14, it can be concluded that both the 38% plastic pre-straining and hydrogen charging of the studied 316H material result in hardening effects in terms of the increase in micro-hardness and nano-hardness. Obviously, the effect of plastic pre-strain is far more significant than the effect of pure hydrogen charging. This observation qualitatively agrees with the

results of uniaxial tensile tests presented in Figure 8, i.e., it also demonstrates that the hardening (strengthening) effect due to the hydrogen charging does not strongly depend on the application of the plastic pre-strain, as quite similar hydrogen hardening effects are observed for both the as-received and 38% plastically pre-strained materials (Figure 14).

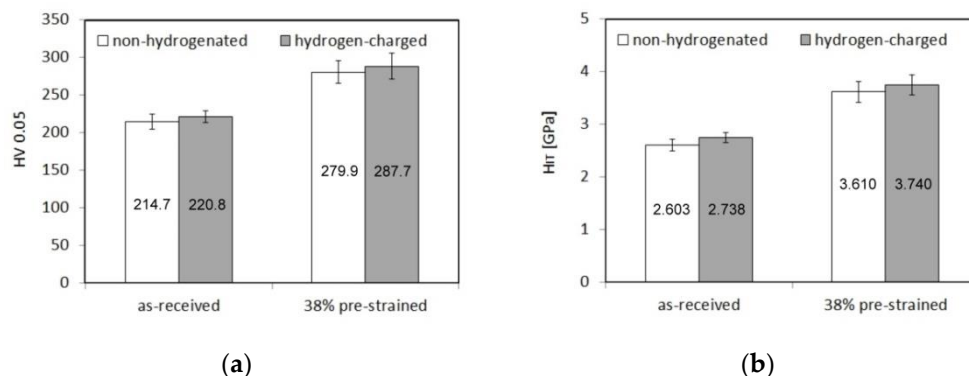


Figure 14. The effects of plastic pre-straining and cathodic hydrogen charging of studied 316H material on its: (a) micro-hardness and (b) nano-hardness.

In correlation with these findings, it can also be concluded that the higher measure of degradation of deformation properties of 38% plastically pre-strained 316H materials (Figure 9) is rather caused by the effect of plasticity exhaustion at the UTS point than by the effect of HE. The obtained results have clearly shown that the studied solution-annealed 316H material in both the as-received and plastically pre-strained material states exhibits good resistance to HE under applied tensile pre-straining and electrochemical hydrogen charging conditions.

4. Conclusions

This work dealt with investigation of the effects of plastic pre-strain and subsequent electrochemical hydrogen charging on the hydrogen embrittlement behavior of solution-annealed 316H stainless steel. Here are the main conclusions:

- The performed XRD and EBSD phase analyses indicated a fully austenitic, i.e., FCC, crystal structure of the studied material in its as-received solution-annealed material condition. The EBSD microstructural analysis revealed that the single-phase microstructure was mainly formed of randomly distributed polygonal grains showing the occasional occurrence of annealing twins.
- For the initial (as-received) material condition, i.e., without the application of plastic pre-strain, a slight increase in strength properties and a certain observable decrease in deformation properties were observed for cathodically hydrogen-charged specimens, compared to the nonhydrogenated ones.
- According to the calculated embrittlement indices, the overall embrittlement of the studied material due to hydrogen was found to be small. This behavior has been ascribed to the high storage of plasticity of the studied material due to its FCC crystal structure and also to its beneficial diffusional characteristics.
- No strain-induced or hydrogen-induced phase transformations were observed in plastically pre-strained and hydrogen-charged material states. With the increasing level of plastic pre-strain up to 38%, a clear decrease in average deformation properties of hydrogen-charged materials was observed. This behavior has been attributed to the strain-induced microstructural changes, specifically the formation of slip dislocations and deformation twins serving as the newly formed hydrogen diffusion paths.
- It has been revealed that the observed degradation of deformation properties of the pre-strained and hydrogen-charged materials was predominantly caused by gradual plasticity exhaustion due to tensile straining, which agreed well with the performed EBSD analyses and micro/nano-hardness measurements.

Author Contributions: Conceptualization, L.F.; methodology, L.Č., I.P. and O.M.; formal analysis, L.F.; investigation, L.F., L.Č., M.D. and K.K.; data curation, L.Č., I.P. and O.M.; writing—original draft preparation, L.F. and L.Č.; writing—review and editing, L.F. and L.Č.; visualization, L.Č.; supervision, L.F.; project administration, L.F.; funding acquisition, L.F. All authors have read and agreed to the published version of the manuscript.

Funding: This research was funded by “Vedecká Grantová Agentúra MŠVVaŠ SR a SAV” (Grant No.: VEGA 2/0072/22).

Institutional Review Board Statement: Not applicable.

Informed Consent Statement: Not applicable.

Data Availability Statement: Not applicable.

Conflicts of Interest: The authors declare no conflict of interest. The funders had no role in the design of the study; in the collection, analyses, or interpretation of data; in the writing of the manuscript; or in the decision to publish the results.

References

1. Miller, B.D.; Webb, T.W. Understanding the effect of crack tip deformation on fatigue crack growth behavior in 300-series austenitic stainless steel. *Int. J. Fatigue* **2019**, *125*, 261–270. [[CrossRef](#)]
2. Park, W.S.; Yoo, S.W.; Kim, M.H.; Lee, J.M. Strain-rate effects on the mechanical behavior of the AISI 300 series of austenitic stainless steel under cryogenic environments. *Mater. Des.* **2010**, *31*, 3630–3640. [[CrossRef](#)]
3. Sudesh, T.L.; Wijesinghe, L.; Blackwood, D.J. Characterisation of passive films on 300 series stainless steels. *App. Surf. Sci.* **2006**, *253*, 1006–1009. [[CrossRef](#)]
4. Yasa, E.; Karasoglu, M. Effect of thickness and build direction on the mechanical behavior and microstructure of AISI 316L stainless steel produced by Laser Beam Powder Bed Fusion. *Kov. Mater.* **2022**, *60*, 55–65. [[CrossRef](#)]
5. Dziubińska, A.; Surdacki, P.; Winiarski, G.; Bulzak, T.; Majerski, K.; Piasta, M. Analysis of the New Forming Process of Medical Screws with a Cylindrical Head of 316 LVM Steel. *Materials* **2021**, *14*, 710. [[CrossRef](#)] [[PubMed](#)]
6. El-Tahawy, M.; Jenei, P.; Kolonits, T.; Han, G.; Park, H.; Choe, H.; Gubicza, J. Different Evolutions of the Microstructure, Texture, and Mechanical Performance During Tension and Compression of 316L Stainless Steel. *Metall. Mat. Trans. A* **2020**, *51*, 3447–3460. [[CrossRef](#)]
7. Wu, Y.; Sun, Z.; Brisset, F.; Baudin, T.; Helbert, A.L.; Retraint, D. In-situ EBSD investigation of thermal stability of a 316L stainless steel nanocrystallized by Surface Mechanical Attrition Treatment. *Mater. Lett.* **2020**, *263*, 127249. [[CrossRef](#)]
8. Ostovan, F.; Shafiei, E.; Toozandehjani, M.; Mohamed, I.F.; Soltani, M. On the role of molybdenum on the microstructural, mechanical and corrosion properties of the GTAW AISI 316 stainless steel welds. *J. Mater. Res. Technol.* **2021**, *13*, 2115–2125. [[CrossRef](#)]
9. Whittaker, M.T.; Evans, M.; Wilshire, B. Long-term creep data prediction for type 316H stainless steel. *Mater. Sci. Eng. A* **2012**, *552*, 145–150. [[CrossRef](#)]
10. Warren, A.D.; Griffiths, I.J.; Flewitt, P.E.J. Precipitation within localised chromium-enriched regions in a Type 316H austenitic stainless steel. *J. Mater. Sci.* **2018**, *53*, 6183–6197. [[CrossRef](#)] [[PubMed](#)]
11. Githinji, D.N.; Northover, S.M.; Bouchard, P.J.; Rist, M.A. An EBSD Study of the Deformation of Service-Aged 316 Austenitic Steel. *Metall. Mater. Trans. A* **2013**, *44*, 4150–4167. [[CrossRef](#)]
12. Hu, J.; Green, G.; Hogg, S.; Higginson, R.; Cocks, A. Effect of microstructure evolution on the creep properties of a polycrystalline 316H austenitic stainless steel. *Mater. Sci. Eng. A* **2020**, *772*, 138787. [[CrossRef](#)]
13. Zhou, H.; Mehmanparast, A.; Nikbin, K. Determination of Long-Term Creep Properties for 316H Steel Using Short-Term Tests on Pre-strained Material. *Exp. Tech.* **2021**, *45*, 549–560. [[CrossRef](#)]
14. Bystrianský, V.; Krausová, A.; Macák, J.; Děd, J.; Eltai, E.; Hamouda, A.M. Beneficial effect of shot peening on steamside oxidation of 300-series austenitic steels: An electrochemical study. *App. Surf. Sci.* **2018**, *427*, 680–685. [[CrossRef](#)]
15. Wang, Y.Q.; Spindler, M.W.; Truman, C.E.; Smith, D.J. Critical analysis of the prediction of stress relaxation from forward creep of Type 316H austenitic stainless steel. *Mater. Des.* **2016**, *95*, 656–668. [[CrossRef](#)]
16. Barnard, P. 4—Austenitic Steel Grades for Boilers in Ultra-Supercritical Power Plants. In *Materials for Ultra-Supercritical and Advanced Ultra-Supercritical Power Plants*; Elsevier: Amsterdam, The Netherlands, 2017; pp. 99–119. [[CrossRef](#)]
17. Warren, A.D.; Griffiths, I.J.; Harniman, R.L.; Flewitt, P.E.J.; Scott, T.B. The role of ferrite in Type 316H austenitic stainless steels on the susceptibility to creep cavitation. *Mater. Sci. Eng. A* **2015**, *635*, 59–69. [[CrossRef](#)]
18. Martinez-Ubeda, A.I.; Griffiths, I.; Karunaratne, M.S.A.; Flewitt, P.E.J.; Younes, C.; Scott, T. Influence of nominal composition variation on phase evolution and creep life of Type 316H austenitic stainless steel components. *Procedia Struct. Integr.* **2016**, *2*, 958–965. [[CrossRef](#)]

19. He, S.; Shang, H.; Fernández-Caballero, A.; Warren, A.D.; Knowles, D.M.; Flewitt, P.E.J.; Martin, T.L. The role of grain boundary ferrite evolution and thermal aging on creep cavitation of type 316H austenitic stainless steel. *Mater. Sci. Eng. A* **2021**, *807*, 140859. [[CrossRef](#)]
20. Blach, J.; Falat, L.; Ševc, P. The influence of hydrogen charging on the notch tensile properties and fracture behavior of dissimilar weld joints of advanced Cr-Mo-V and Cr-Ni-Mo creep-resistant steels. *Eng. Fail. Anal.* **2011**, *18*, 485–491. [[CrossRef](#)]
21. Falat, L.; Svoboda, M.; Vyrostková, A.; Petryshynets, I.; Sopko, M. Microstructure and creep characteristics of dissimilar T91/TP316H martensitic/austenitic welded joint with Ni-based weld metal. *Mater. Charact.* **2012**, *72*, 15–23. [[CrossRef](#)]
22. Falat, L.; Homolová, V.; Kepič, J.; Svoboda, M.; Výrostková, A. Microstructure and properties degradation of P/T 91, 92 steels weldments in creep conditions. *J. Min. Metall. Sect. B Metall.* **2012**, *48*, 461–469. [[CrossRef](#)]
23. Blach, J.; Falat, L. The influence of thermal exposure and hydrogen charging on the notch tensile properties and fracture behaviour of dissimilar T91/TP316H weldments. *High Temp. Mater. Processes* **2014**, *33*, 329–337. [[CrossRef](#)]
24. Falat, L.; Čiripová, L.; Kepič, J.; Buršík, J.; Podstranská, I. Correlation between microstructure and creep performance of martensitic/austenitic transition weldment in dependence of its post-weld heat treatment. *Eng. Fail. Anal.* **2014**, *40*, 141–152. [[CrossRef](#)]
25. Falat, L.; Kepič, J.; Čiripová, L.; Ševc, P.; Dlouhý, I. The effects of postweld heat treatment and isothermal aging on T92 steel heat-affected zone mechanical properties of T92/TP316H dissimilar weldments. *J. Mat. Res.* **2016**, *31*, 1532–1543. [[CrossRef](#)]
26. Čiripová, L.; Falat, L.; Ševc, P.; Vojtko, M.; Džupon, M. Ageing effects on room temperature tensile properties and fracture behavior of quenched and tempered T92/TP316H dissimilar welded joints with Ni-based weld metal. *Metals* **2018**, *8*, 791. [[CrossRef](#)]
27. Ševc, P.; Falat, L.; Čiripová, L.; Džupon, M.; Vojtko, M. The effects of electrochemical hydrogen charging on room-temperature tensile properties of T92/TP316H dissimilar weldments in quenched-and-tempered and thermally-aged conditions. *Metals* **2019**, *9*, 864. [[CrossRef](#)]
28. Manimozhi, S.; Suresh, S.; Muthupandi, V. HAZ hydrogen cracking of 9Cr-0.5 Mo-1.7W steels. *Int. J. Adv. Manuf. Technol.* **2010**, *51*, 217–223. [[CrossRef](#)]
29. Hadžipašić, A.B.; Malina, J.; Malina, M. The influence of microstructure on hydrogen diffusion and embrittlement of fine-grained high strength dual-phase steels. *Kov. Mater.* **2021**, *59*, 69–78. [[CrossRef](#)]
30. Eliezer, D. The behavior of 316L stainless steel in hydrogen. *J. Mater. Sci.* **1984**, *19*, 1540–1547. [[CrossRef](#)]
31. Herms, E.; Olive, J.M.; Puiggali, M. Hydrogen embrittlement of 316L type stainless steel. *Mater. Sci. Eng. A* **1999**, *272*, 279–283. [[CrossRef](#)]
32. Lee, S.K.; Kim, H.S.; Noh, S.J. Hydrogen Permeability, Diffusivity, and Solubility of SUS 316L Stainless Steel in the Temperature Range 400 to 800 °C for Fusion Reactor Applications. *J. Korean Phys. Soc.* **2011**, *59*, 3019–3023. [[CrossRef](#)]
33. Omura, T.; Nakamura, J. Hydrogen Embrittlement Properties of Stainless and Low Alloy Steels in High Pressure Gaseous Hydrogen Environment. *ISIJ Int.* **2012**, *52*, 234–239. [[CrossRef](#)]
34. Ogata, T. Influence of high pressure hydrogen environment on tensile and fatigue properties of stainless steels at low temperatures. *AIP Conf. Proc.* **2012**, *1435*, 39–46. [[CrossRef](#)]
35. Michler, T.; Naumann, J.; Hock, M.; Berreth, K.; Balogh, M.P.; Sattler, E. Microstructural properties controlling hydrogen environment embrittlement of cold worked 316 type austenitic stainless steels. *Mater. Sci. Eng. A* **2015**, *628*, 252–261. [[CrossRef](#)]
36. Bak, S.H.; Kim, S.S.; Lee, D.B. Effect of hydrogen on dislocation structure and strain-induced martensite transformation in 316L stainless steel. *RSC Adv.* **2017**, *7*, 27840–27845. [[CrossRef](#)]
37. Nicho, K.; Yokoyama, K. Marked Degradation of Tensile Properties Induced by Plastic Deformation after Interactions between Strain-Induced Martensite Transformation and Hydrogen for Type 316L Stainless Steel. *Metals* **2020**, *10*, 928. [[CrossRef](#)]
38. Khaleghifar, F.; Razeghi, K.; Heidarzadeh, A.; Mousavian, R.T. Effect of Hydrogen on the Tensile Behavior of Austenitic Stainless Steels 316L Produced by Laser-Powder Bed Fusion. *Metals* **2021**, *11*, 586. [[CrossRef](#)]
39. Bertsch, K.M.; Nagao, A.; Rankouhi, B.; Kuehl, B.; Thoma, D.J. Hydrogen embrittlement of additively manufactured austenitic stainless steel 316 L. *Corros. Sci.* **2021**, *192*, 109790. [[CrossRef](#)]
40. Nygren, K.E.; Nagao, A.; Wang, S.; Sofronis, P.; Robertson, I.M. Influence of internal hydrogen content on the evolved microstructure beneath fatigue striations in 316L austenitic stainless steel. *Acta Mater.* **2021**, *213*, 116957. [[CrossRef](#)]
41. Murakami, Y.; Kanezaki, T.; Mine, Y.; Matsuoka, S. Hydrogen Embrittlement Mechanism in Fatigue of Austenitic Stainless Steels. *Metal. Mater. Trans. A* **2008**, *39*, 1327–1339. [[CrossRef](#)]
42. Yang, F.; Yan, T.; Zhang, W.; Zhang, H.; Zhao, L. Modeling the Hydrogen Redistribution at the Grain Boundary of Misoriented Bicrystals in Austenite Stainless Steel. *Materials* **2022**, *15*, 479. [[CrossRef](#)] [[PubMed](#)]
43. Nguyen, T.T.; Park, J.; Nahm, S.H.; Baek, U.B. An experimental study for qualifying hydrogen compatibility of austenitic stainless steel under low temperature. *J. Mech. Sci. Technol.* **2022**, *36*, 157–165. [[CrossRef](#)]
44. Nguyen, L.T.H.; Hwang, J.-S.; Kim, M.-S.; Kim, J.-H.; Kim, S.-K.; Lee, J.-M. Charpy impact properties of hydrogen-exposed 316L stainless steel at ambient and cryogenic temperatures. *Metals* **2019**, *9*, 625. [[CrossRef](#)]
45. Jia, H.; Zhang, X.; Xu, J.; Sun, Y.; Li, J. Effect of hydrogen content and strain rate on hydrogen-induced delay cracking for hot-stamped steel. *Metals* **2019**, *9*, 798. [[CrossRef](#)]

46. Dunne, D.P.; Hejazi, D.; Saleh, A.A.; Haq, A.J.; Calka, A.; Pereloma, E.V. Investigation of the effect of electrolytic hydrogen charging of X70 steel: I. The effect of microstructure on hydrogen-induced cold cracking and blistering. *Int. J. Hydrog. Energy* **2016**, *41*, 12411–12423. [[CrossRef](#)]
47. Yin, C.; Chen, J.; Ye, D.; Xu, Z.; Ge, J.; Zhou, H. Hydrogen concentration distribution in 2.25cr-1mo-0.25v steel under the electrochemical hydrogen charging and its influence on the mechanical properties. *Materials* **2020**, *13*, 2263. [[CrossRef](#)]
48. *ISO 6507-1:2018*; Metallic materials—Vickers hardness test—Part 1: Test method. ISO: London, UK, 2018. Available online: <https://www.iso.org/standard/64065.html> (accessed on 26 September 2022).
49. *ISO 14577-1:2015*; Metallic materials—Instrumented indentation test for hardness and materials parameters—Part 1: Test method. ISO: London, UK, 2015. Available online: <https://www.iso.org/standard/56626.html> (accessed on 26 September 2022).
50. Krom, A.H.M.; Bakker, A. Hydrogen trapping models in steel. *Metall. Mater. Trans. B* **2000**, *31*, 1475–1482. [[CrossRef](#)]
51. Gao, C.Y.; Zhang, L.C. A constitutive model for dynamic plasticity of FCC metals. *Mater. Sci. Eng. A* **2010**, *527*, 3138–3143. [[CrossRef](#)]
52. Jo, M.; Koo, Y.M.; Lee, B.J.; Johansson, B.; Vitos, L.; Kwon, S.K. Theory for plasticity of face-centered cubic metals. *Proc. Natl. Acad. Sci. USA* **2014**, *111*, 6560–6565. [[CrossRef](#)] [[PubMed](#)]
53. Vökl, J.; Alefeld, G. Diffusion of Hydrogen in Metals. In *Hydrogen in Metals I*; Topics in Applied Physics; Springer: Berlin/Heidelberg, Germany, 1978; Volume 28, pp. 321–348. [[CrossRef](#)]
54. Feng, Z.; Li, X.; Song, X.; Gu, T.; Zhang, Y. Hydrogen Embrittlement of CoCrFeMnNi High-Entropy Alloy Compared with 304 and IN718 Alloys. *Metals* **2022**, *12*, 998. [[CrossRef](#)]
55. Zhou, Y.; Zhou, D.; Jin, X.; Zhang, L.; Du, X.; Li, B. Design of non-equiatomic medium-entropy alloys. *Sci. Rep.* **2018**, *8*, 1236. [[CrossRef](#)] [[PubMed](#)]
56. Zhang, X.-F.; Kan, Z.-W.; Yang, Y.; Wan, Y.-X.; Li, J.-X.; Huang, Z.-Y. Investigation of the effect of electrolytic hydrogen charging on tensile-ductility loss in different Al-added low density steels. *Mater. Sci. Eng. A* **2020**, *795*, 140027. [[CrossRef](#)]
57. Gathimba, N.; Kitane, Y. Effect of surface roughness on tensile ductility of artificially corroded steel plates. *J. Constr. Steel Res.* **2021**, *176*, 106392. [[CrossRef](#)]